

Heating of the molecular gas in the massive outflow of the local ultraluminous-infrared and radio-loud galaxy 4C12.50

K. M. Dasyra¹, F. Combes¹, G. S. Novak¹, M. Bremer², L. Spinoglio³, M. Pereira Santaella³, P. Salomé¹, and E. Falgarone¹

¹ Observatoire de Paris, LERMA (UMR8112), 61 Av. de l'Observatoire, F-75014, Paris, France

² Institut de Radio Astronomie Millimétrique, 300 rue de la Piscine, F-38406 Saint-Martin d'Hères, France

³ Istituto di Astrofisica e Planetologia Spaziali, INAF-IAPS, Via Fosso del Cavaliere 100, I-00133 Roma, Italy

ABSTRACT

We present a comparison of the molecular gas properties in the outflow vs. in the ambient medium of the local prototype radio-loud and ultraluminous-infrared galaxy 4C12.50 (IRAS13451+1232), using new data from the IRAM Plateau de Bure interferometer and 30 m telescope, and the *Herschel* space telescope. Previous H₂ (0-0) S(1) and S(2) observations with the *Spitzer* space telescope had indicated that the warm (~ 400 K) molecular gas in 4C12.50 is made up of a $1.4(\pm 0.2) \times 10^8 M_\odot$ ambient reservoir and a $5.2(\pm 1.7) \times 10^7 M_\odot$ outflow. The new CO(1-0) data cube indicates that the corresponding cold (25 K) H₂ gas mass is $1.0(\pm 0.1) \times 10^{10} M_\odot$ for the ambient medium and $< 1.3 \times 10^8 M_\odot$ for the outflow, when using a CO-intensity-to-H₂-mass conversion factor α of $0.8 M_\odot / (\text{K km s}^{-1} \text{ pc}^2)$. The combined mass outflow rate is high, 230-800 M_\odot/yr , but the amount of gas that could escape the galaxy is low. A potential inflow of gas from a $3.3(\pm 0.3) \times 10^8 M_\odot$ tidal tail could moderate any mass loss. The mass ratio of warm-to-cold molecular gas is $\gtrsim 30$ times higher in the outflow than in the ambient medium, indicating that a non-negligible fraction of the accelerated gas is heated to temperatures at which star formation is inefficient. This conclusion is robust against the use of different α factor values, and/or different warm gas tracers (H₂ vs. H₂ plus CO): with the CO-probed gas mass being at least 40 times lower at 400 K than at 25 K, the total warm-to-cold mass ratio is always lower in the ambient gas than in the entrained gas. Heating of the molecular gas could facilitate the detection of new outflows in distant galaxies by enhancing their emission in intermediate rotational number CO lines.

Key words. ISM: jets and outflows — ISM: kinematics and dynamics — Line: profiles — Galaxies: active — Galaxies: nuclei — Infrared: galaxies

1. Introduction

Mass accretion events onto black holes (BHs) can release more energy than the binding energy of gas in galaxies (Fabian, 2012), and part of this energy can be deposited onto the interstellar medium (ISM) through radiation, accretion-disk winds, and radio jets. The energy carried by these so-called feedback mechanisms can excite or kinematically distort gas on large scales (e.g., over areas of square kiloparsecs; Lípari et al., 2004; Fu & Stockton, 2009; Rupke & Veilleux, 2011; Westmoquette et al., 2012). It can even affect galaxies external to the active galactic nucleus (AGN) that generated it (e.g., Croft et al., 2006; Cantalupo et al., 2012). The effects of feedback on the evolution of galaxies are most severe if part of the gas is accelerated beyond escape velocity. The high-velocity gas will then be lost to the intergalactic medium. Any star formation associated with it will be quenched. For the remaining gas, star formation will be delayed. The low-velocity gas will cool radiatively, resettle in a disk, and restart its collapse towards the formation of new cores. For these reasons, AGN feedback has been considered as a source of negative feedback, capable of regulating galaxy growth. Positive feedback, i.e., compression of gas leading to an enhancement of star formation has also been occasionally suggested (e.g., van Breugel et al., 1985; Gaibler et al., 2012; Silk, 2013).

AGN feedback, implemented either as a source of heating coupled to the hot gas or as a source of momentum coupled to the cold gas, was included in cosmological simulations to suppress star formation at earlier epochs and to make the predicted number counts of massive present-day galaxies match the observed ones (Granato et al., 2004; Croton et al., 2006; Bower et al., 2006; Somerville et al., 2008; Booth & Schaye, 2009; Debuhr et al., 2012). The claim that feedback could change the high-mass end of the local galaxy mass function by more than an order of magnitude was however contested by Birnboim et al. (2007), Dekel & Birnboim (2008), and Bernardi et al. (2013), who argued that the numbers could be revised downwards through, e.g., different stellar population modeling assumptions.

The change in the galaxy mass function by AGN feedback remains to be quantified or constrained by observations. To quantify it, we need to determine the frequency of AGN-driven outflows that can considerably delay or quench star formation in their host galaxies. Even though high-velocity outflows have long been identified in optical and radio data of ionized and neutral atomic gas tracers in local AGN (e.g., Heckman et al., 2000; Rupke et al., 2005; Martin, 2005; Morganti et al., 2005; Holt et al., 2008), this research field became particularly appealing thanks to the launch of infrared (IR) space missions (e.g., *Herschel*) and

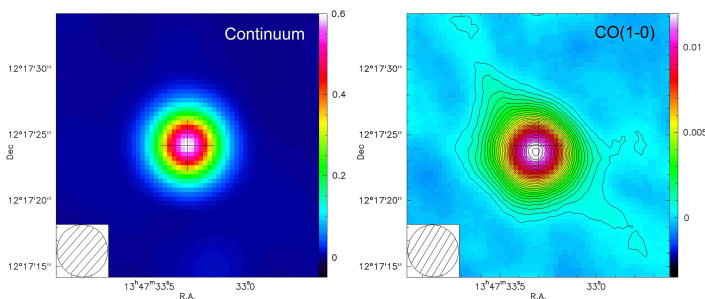


Fig. 1. *Left:* 102 GHz continuum image of 4C12.50 (in units of Jy/beam). *Right:* Continuum-free CO(1-0) line intensity map of 4C12.50 averaged over the -500 km s^{-1} to 500 km s^{-1} range, showing extended emission that is offset from the continuum peak (marked with a cross). The contours are at the 3σ levels for this image, i.e., at steps of 0.36 mJy/beam .

the improvement on the sensitivity and the spectral range of ground-based mm facilities, which enabled us to probe the molecular gas content of outflows. Being the densest ISM component, the molecular gas can considerably contribute to the mass of the entrained gas, if not dominate it. Motions of molecular gas that could be associated with a nuclear outflow have been presented for ~ 50 local galaxies to date (Sakamoto et al., 2006, 2009; Leon et al., 2007; Feruglio et al., 2010; Fischer et al., 2010; Alatalo et al., 2011; Rangwala et al., 2011; Sturm et al., 2011; Krips et al., 2011; Dasyra & Combes, 2011, 2012; Aalto et al., 2012; Tsai et al., 2012; Morganti et al., 2013a; Combes et al., 2013; Spoon et al., 2013; Veilleux et al., 2013; Ciccone et al., 2014). Mass measurements of the accelerated gas were presented in \sim one fifth of the cases and found to be in the range 10^6 – $10^9 M_{\odot}$.

To identify spectral lines with strong outflow signatures, and use them for the systematic and efficient detection of new outflows, we need to perform excitation studies of the gas in the flow, motivated by the argument that the AGN feedback could leave both kinematic and excitation signatures on the ISM. Such studies have nonetheless only been presented for a couple of sources. In Mrk 231, Ciccone et al. (2012) found no evidence for a strong contribution of shocks on the excitation of outflowing CO molecules at states of low rotational number J : the CO(2-1)/CO(1-0) flux ratio was comparable in the outflow and in the ambient medium.

In this paper, we present evidence of heating of the molecular gas in the outflow of the local radio-loud and ultraluminous-infrared system 4C12.50 (IRAS 13451+1232), i.e., a late-stage merger of two galaxies where the nuclei are separated by 4.4 kpc and surrounded by smaller structures (Batcheldor et al., 2007). A relativistic radio jet with an intrinsic bulk flow speed of at least $0.8c$ emerges from the system’s west nucleus (Lister et al., 2003). The setup of a radio jet propagating through a gas-rich galaxy, which is rare in the local Universe but common at high redshift (e.g., Sajina et al., 2008; Ivison et al., 2012), makes 4C12.50 an excellent target for studying the properties of the outflowing molecular gas. The uniqueness of 4C12.50 lies in the discovery and the characterization of a warm molecular gas outflow in it: it was the only source in the *Spitzer* archive for which an outflow-related wing was detected in two purely rotational H_2 lines, providing the entrained gas excitation temperature and mass (Dasyra &

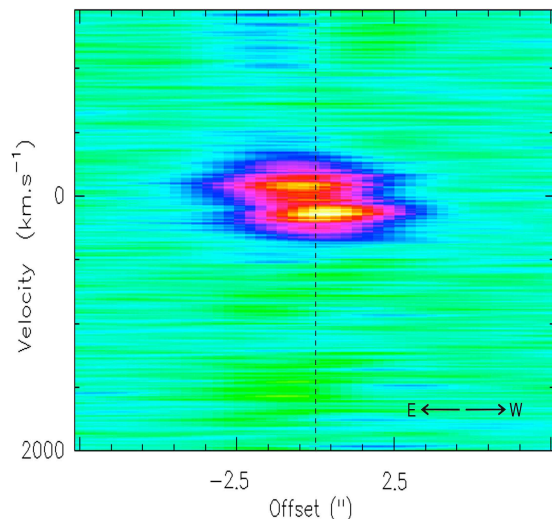


Fig. 2. Position-velocity diagram of the continuum-free CO(1-0) emission along the east-west axis, displayed for a velocity resolution of 6 km s^{-1} . The x-axis offset is computed from the radio core location, which is marked with a dashed line. The offset increases (/decreases) towards the west (/east).

Combes, 2011). Cold gas was also discovered in the outflow thanks to absorption seen in CO(2-3) with a significant optical depth against the millimeter continuum source (Dasyra & Combes, 2012). In this paper, we compare the properties of the gas in the outflow vs. that in the ambient medium using new submillimeter and millimeter data, and we discuss the implications of our findings for future searches of massive molecular gas outflows. Throughout our work, we adopt a Λ CDM cosmology with $H_0 = 70 \text{ km s}^{-1} \text{ Mpc}^{-1}$, $\Omega_M = 0.3$, and $\Omega_{\Lambda} = 0.7$.

2. Data

The CO(1-0) observations were carried out with the Plateau de Bure (PdB) Interferometer of the Institut de Radioastronomie Millimétrique (IRAM) as part of the program V028 (PI Dasyra). The data were taken on four different days between September 2011 and January 2012, during which four, five, or six antennae were placed in compact (C, D, or special) configurations. The dual polarization SIS receivers were tuned at a frequency ν of 102.761 GHz , and used with the WIDEX backend. The typical weather conditions were 0.6 – $2.2''$ of seeing and 2 – 10 mm of water vapor. Bandpass calibrators (0923+392, 1354+195, 3C84, 3C279) were observed before our primary target during the first two runs. During the next two runs, they were observed before and after each 22.5 minute-long integration on 4C12.50. This change to the observational strategy enabled us to minimize the scatter due to the strong millimeter continuum of 4C12.50 by monitoring changes in the time-variable bandpass solution and thus increasing the accuracy of the subsequent phase and flux calibrations. To perform the latter two tasks, we used the default IRAM environment, CLIC¹, selecting 4C12.50 itself for the phase calibration and MWC 349 for the flux calibration. The calibrated visibilities of all tracks were merged into a single table, of depth equivalent to 12.5 hours of observations with

¹ <http://www.iram.fr/IRAMFR/GILDAS>

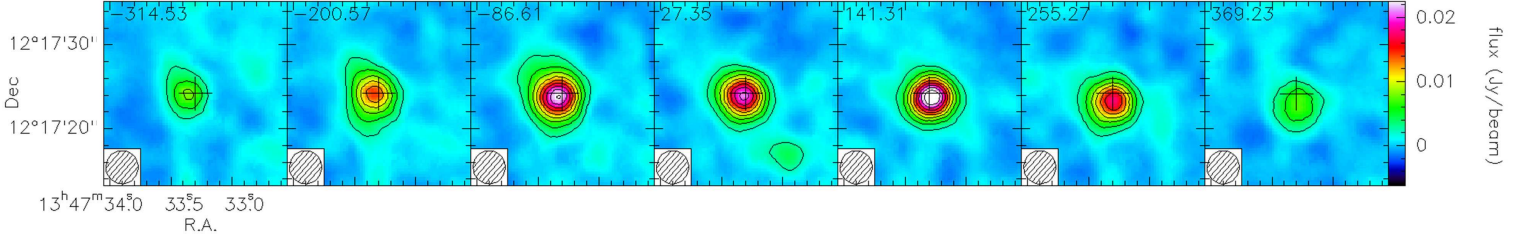


Fig. 3. Continuum-free CO(1-0) line intensity map of 4C12.50, displayed for ~ 114 km s^{-1} bins (in the range -315 km s^{-1} to 369 km s^{-1}). The number at the upper-left corner of each frame corresponds to the bin mean velocity. Contours are plotted at integer multiples of the 5σ level for these images, i.e., at steps of 2.4 mJy/beam . A shift towards the west of the line peak position from negative to positive velocities, as well as a distinct kinematic component near rest-frame velocity are observed.

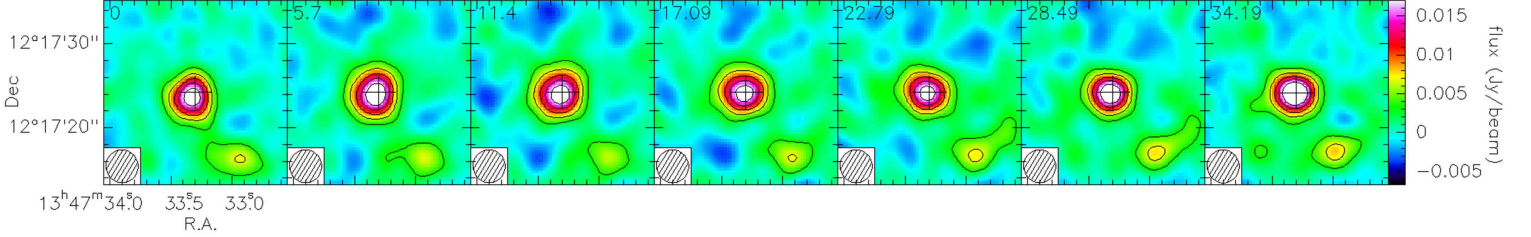


Fig. 4. Same as in Fig. 3, but for bins of 17 km s^{-1} (in the range 0 to 34 km s^{-1}). Contours are plotted at integer multiples of the 3.5σ level for these images, i.e., at steps of 3.3 mJy/beam .

a six-antenna array. A cube of $0.34''$ per spatial pixel was created from this table using the default PdB image reconstruction environment, MAPPING¹. Its 1σ noise is 1.1 mJy per beam at a spectral resolution of 5.7 km s^{-1} . The clean 3 mm beam corresponds to an ellipse with semi-major and semi-minor axis of $4.0''$ and $3.8''$, respectively, at a position angle of 14° . We constructed the continuum image by computing the median of all cube planes in the 450 km s^{-1} to 1250 km s^{-1} range, and removed it from the entire cube to obtain a continuum-free CO(1-0) line cube (Figure 1).

Observations at 205.522 GHz targeting the CO(2-1) line were carried out in June 2012 with the IRAM 30 m telescope. The Eight Mixer Receiver (EMIR; Carter et al., 2012) and the Wideband Line Multiple Autocorrelator (WILMA) backend were used for this program. The FTS backend was also connected for repeatability. The data presented here are rather shallow, of 20 minutes of on-source integration time, taken while the 1.5 mm system temperature varied from 400 to 450 K. The deterioration of the weather conditions prevented the acquisition of more data. The individual scans were examined, stacked, and binned to 47 km s^{-1} channels within the CLASS environment¹.

We followed up 4C12.50 with the PACS (Poglitsch et al., 2010) far-infrared instrument on board *Herschel* (Pilbratt et al., 2010) to look for emission from CO molecules that are excited to states of high rotational number. High spectral sampling CO(16-15) observations were carried out for our GT2_lspinogl_6 program in range-spectroscopy mode using chop-nod cycles. To populate the CO spectral line energy distribution (SLED), we combined our data with all PACS range or line spectroscopy data in the *Herschel* archive that cover the observed-frame wavelengths of CO lines in 4C12.50. For this reason, we examined the blue array data and their parallel red array data in each astronomical observation request (AOR). We found that, in total, information is available for four transitions, CO(33-32), CO(22-

21), CO(18-17), and CO(16-15), with integration times of 1.2, 4.0, 1.4, and 2.1 hours, respectively. For CO(22-21), this is the total time of the combined OT1_dfarrah_1 and OT1_sveilleu_3 program data. We reduced the data within the *Herschel* Interactive Processing Environment (HIPE; version 8.3, calibration tree version 32; Ott et al. 2010), by running the default PACS spectrometer pipeline for chopped-line and short-range scans with a wavelength grid oversampling parameter² of 2. We flagged as outliers all pixel read-outs in emission-line-free wavelengths whose flux exceeded 5σ . Because 4C12.50 is a point source for PACS, we obtained its final spectrum at each wavelength by extracting the spectrum of the central $9.4'' \times 9.4''$ spaxel of each data cube, and by multiplying it by the point-source-correction factor in order to recover its full flux. We followed an identical procedure to reduce all other archival PACS observations of 4C12.50 in order to obtain information on its far-infrared dust continuum emission. From this process, we excluded AORS in spectral ranges that suffer from flux leakage from/to other wavelengths, such as <54 μm , 70 – 74 μm , and 95 – 105 μm .

3. Results

3.1. CO(1-0) data: gas mass and distribution

The median channel with a CO(1-0) detection in the PdB data cube is at 102.756 GHz, pointing to a redshift z of 0.12179 . When adopting this redshift and collapsing the continuum-subtracted cube over the -500 km s^{-1} to 500 km s^{-1} velocity range, we find that the CO(1-0) emission is offset from the 3 mm continuum peak and marginally

² The differences between the spectra obtained by running the default pipeline and the spectra obtained by running the routines for an alternative flux calibration based on the telescope background are within the given error bars.

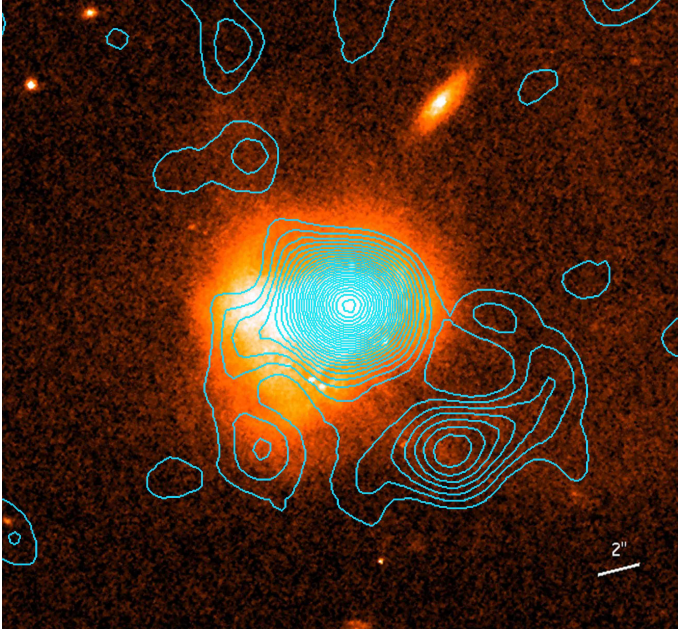


Fig. 5. Contours of the CO(1-0) emission of 4C12.50, integrated from 25 km s^{-1} to 35 km s^{-1} and plotted over an 7300 \AA *Hubble* Space Telescope ACS image (Batcheldor et al., 2007). The contours start at the 1σ level of the collapsed CO(1-0) image, 0.014 Jy/beam . They are spaced by an equal amount.

extended (Figure 1). When examining the data cube within the $-500 < V < 500 \text{ km s}^{-1}$ range, we find that the CO(1-0) emission progresses from the east to the west as the velocity increases from negative to positive values (Figures 2,3). It peaks at two locations, $\sim 1''$ (or $\sim 2.2 \text{ kpc}$) apart. This emission arises from gas that could be associated with the two main merging nuclei of 4C12.50 (Dasyra et al., 2006a), with an off-center disk forming due to the merger, or with a combination of the above.

A distinct, off-center component is also detected in the central velocity bin of Figure 3, at $\sim 10 \text{ kpc}$ south-west of the main nucleus. An inspection of the data cube at a higher spectral resolution (Figure 4) reveals that this component has a tidal structure, approaching the main component at systemic velocity. Its distance from the center progressively increases with increasing velocity, until it reaches 12 kpc at $\sim 30 \text{ km s}^{-1}$. The structure has a faint counterpart in the optical (Figure 5), and it is by far the most gas rich (and thus dust rich) of all tidal tails in this system.

The spectra extracted from the data cube are shown in Figures 6 and 7 for the main component, and Figure 8 for the tidal tail. Figure 6 reveals an asymmetry in the CO(1-0) emission profile along the east-west axis at sub-beam scales that is likely due to the merger. The profile can also be compatible with absorption of CO and continuum emission by molecules at systemic velocity, as, e.g., in Centaurus A (Eckart et al., 1990; Wiklind & Combes, 1997).

To find the mass of the H_2 gas that is associated with the CO emission shown in Figures 7 and 8, we computed the product $3.25 \times 10^7 \alpha S_{\text{CO}(1-0)} \Delta V \nu_{\text{obs}}^{-2} D_L^2 / (1+z)^3 M_{\odot}$, where α is the CO intensity to H_2 mass conversion factor, $S_{\text{CO}(1-0)} \Delta V$ is the integrated line flux in Jy km s^{-1} , ν_{obs} is the observed CO(1-0) frequency in GHz, and D_L is the

source luminosity distance in Mpc (Solomon et al., 1997). We adopted an α value of $0.8 M_{\odot} / (\text{K km s}^{-1} \text{ pc}^2)$, to be consistent with the literature assuming a lower conversion factor for ultraluminous infrared galaxies (ULIRGs) than for the Milky Way (Downes & Solomon, 1998).

For the main emission component (Figures 1, 7), we measure a flux of $18.2 \pm 1.5 \text{ Jy km s}^{-1}$. From this flux we calculate a cold H_2 gas mass reservoir of $1.0 (\pm 0.1) \times 10^{10} M_{\odot}$. Likewise, the flux in the tidal tail is $0.61 \pm 0.04 \text{ Jy km s}^{-1}$ (integrated down to the 1σ level, as shown in Figure 5). This corresponds to an H_2 mass of $3.3 (\pm 0.3) \times 10^8 M_{\odot}$. We thus find that a mass comparable to $1/30^{\text{th}}$ of the main reservoir could be infalling thanks to the tidal tail (see Section 4). Because the total CO(1-0) flux in the PdB data agrees within the error with that previously measured in IRAM 30 m telescope data ($20 \pm 6 \text{ Jy km s}^{-1}$; Dasyra & Combes, 2011), we deduce that the interferometer did not miss a significant part of the extended emission.

A spatially-unresolved absorption line at -720 km s^{-1} at the radio core and less than a handful of emission lines at $V < -500 \text{ km s}^{-1}$ or $V > 500 \text{ km s}^{-1}$ were seen in the PdB data at ~ 3 -5 root mean square noise (σ) levels. Their widths never exceeded $\sim 80 \text{ km s}^{-1}$. These lines could be real (due to a small collection of high-velocity clouds in the outflow), or artifacts (due to the varying position and intensity of the mm continuum, which leads to an inadequate removal of the point spread function). A reliable detection of the outflow in CO(1-0) remains to be achieved with higher dynamic range observations. In the rest of this work, we adopt an upper limit of $1.3 \times 10^8 M_{\odot}$ for the mass of the cold molecular gas in the outflow. We computed this limit by integrating 3σ over the velocity range that the molecular outflow spans in other wavelengths ($-1300 \text{ km s}^{-1} < V < -300 \text{ km s}^{-1}$; Dasyra & Combes 2011, 2012). We further assumed that the outflow is spatially unresolved, constrained within our four-kiloparsec-radius beam. Indeed, no evidence of an extended (ionized gas) outflow was found in multi-slit optical spectra of 4C12.50 (Holt et al., 2008, 2011). The neutral atomic gas component of the outflow observed in the radio is found $\sim 150 \text{ pc}$ away from the nucleus, at the tip of the southern radio hot spot (Morganti et al., 2013b).

3.2. Higher rotational number CO lines

The IRAM 30 m telescope CO(2-1) data (Figure 9) have a beam of $\sim 12''$, which comprises all regions seen in emission in the PdB data. The measured CO(2-1) flux³ was $35 (\pm 6) \text{ Jy km s}^{-1}$, which together with a previously measured CO(3-2) flux of $50 \pm 8 \text{ Jy km s}^{-1}$ (Dasyra & Combes, 2012) indicate a subthermal excitation of the CO molecules. Their excitation up to $J=3$ is identical with that of the gas in the Milky Way, towards the Galactic center, and higher than that in outflow of M82 (Figure 11; Weiss et al., 2001, 2005).

³ The width of the CO(2-1) line in the 30 m telescope data, $390 \pm 68 \text{ km s}^{-1}$, is lower and more uncertain than that of the CO(1-0) line in the PdB data. The uncertainty is due to the sinusoidal baseline in the single-dish data due to standing waves related to the bright continuum of 4C12.50. It does not necessarily translate into a flux loss. For comparison see the different line shape but identical line flux of CO(1-0) obtained with the PdB array and the 30 m telescope (Dasyra & Combes, 2012).

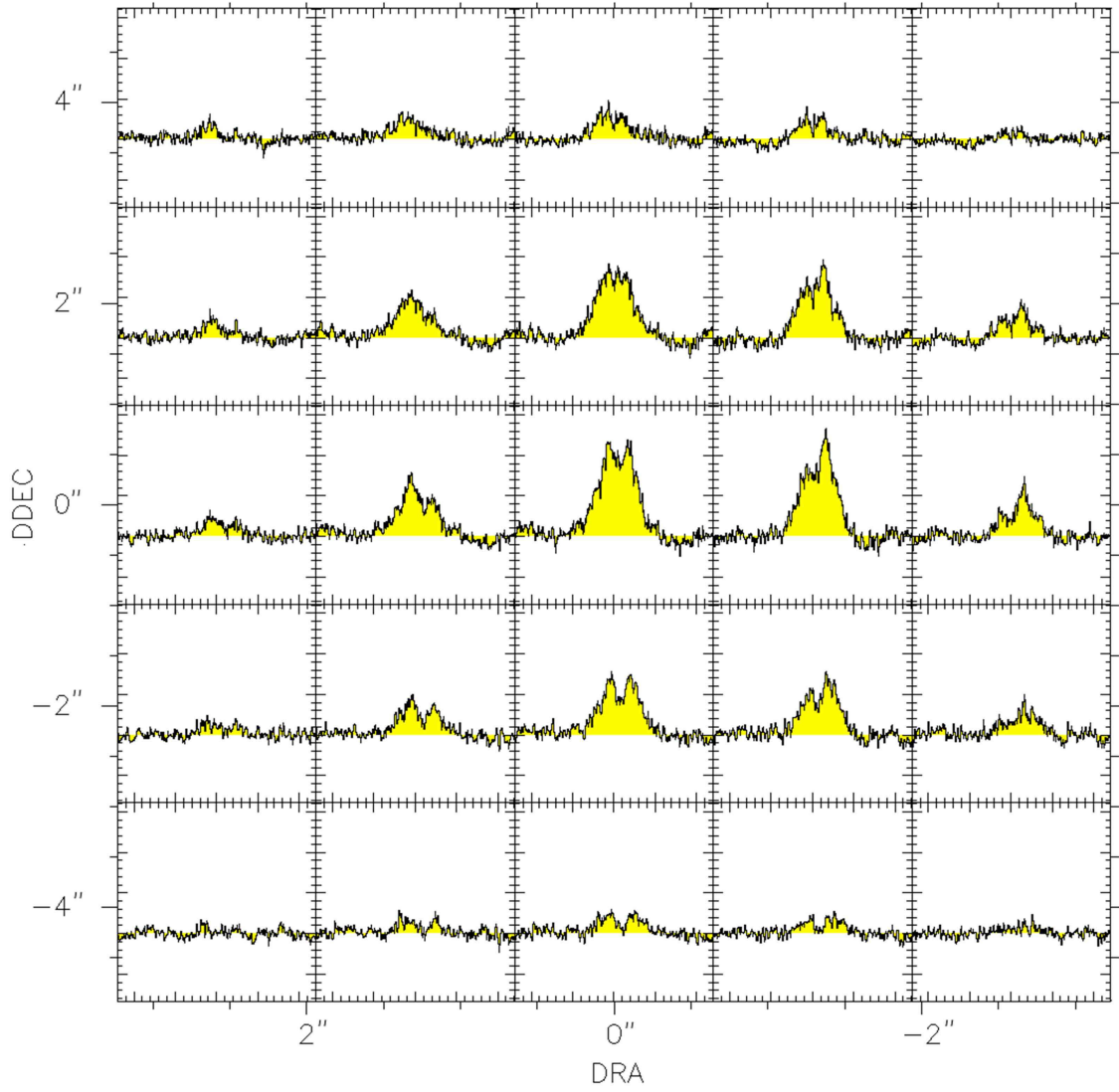


Fig. 6. CO(1-0) line profile changes within few arcseconds (i.e., at sub-beam scales) from the position of the radio core in the PdB data. All spectra are plotted in the -1200 km s^{-1} to 1200 km s^{-1} velocity range.

Table 1. CO Line Observations

Line	$\lambda_{\text{restframe}}$ (μm)	flux ($10^{-18} \text{ W m}^{-2}$)	FWHM (km s^{-1})
CO(1-0)	2600.7	0.064 ± 0.005	517 ± 14
CO(2-1)	1300.4	0.24 ± 0.04	390 ± 68
CO(3-2)	866.96	$0.51 \pm 0.08^{(1)}$	$510 \pm 65^{(1)}$
CO(5-4)	520.23	$< 8.0^{(2)}$...
CO(6-5)	433.55	$< 4.7^{(2)}$...
CO(7-6)	371.65	$< 3.5^{(2)}$...
CO(8-7)	325.22	$< 4.4^{(2)}$...
CO(9-8)	289.12	$< 5.8^{(2)}$...
CO(10-9)	260.24	$< 6.0^{(2)}$...
CO(11-10)	236.61	$< 6.0^{(2)}$...
CO(12-11)	216.93	$< 6.0^{(2)}$...
CO(13-12)	200.27	$< 6.0^{(2)}$...
CO(16-15)	162.81	< 2.5	...
CO(18-17)	144.78	< 1.8	...
CO(22-21)	118.58	0.97 ± 0.27	...
CO(33-32)	79.36	< 5.0	...

⁽¹⁾ Value taken from Dasyra & Combes (2012).

⁽²⁾ Estimated from SPIRE's sensitivity for 2.8 hrs on source.

Table 2. Continuum fluxes in the infrared and mm range

$\lambda_{\text{restframe}}$ (μm)	flux (Jy)
52.0	2.21 ± 0.10
57.5	2.39 ± 0.15
78.7	2.46 ± 0.11
81.0	2.30 ± 0.18
121.0	1.51 ± 0.06
126.0	1.53 ± 0.10
146.0	1.48 ± 0.12
155.0	1.36 ± 0.17
158.5	1.15 ± 0.10
162.5	0.85 ± 0.13
172.0	1.00 ± 0.19
870	0.15 ± 0.02
1305	0.30 ± 0.07
2610	0.51 ± 0.06

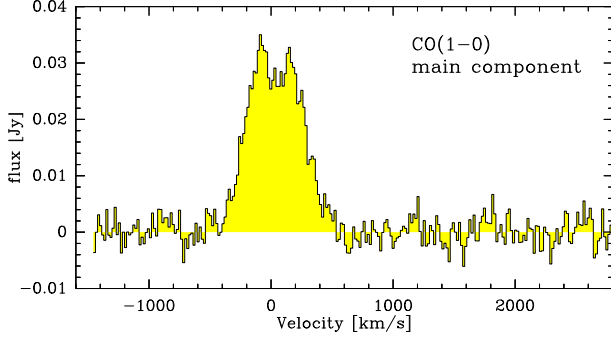


Fig. 7. Line profile of the main CO(1-0) emission component in the PdB data. The flux is integrated down to the 1σ level of the integrated CO(1-0) emission (Figure 1; typically 7-9'' from the radio core), excluding the emission from the tidal structure, which is shown in Figure 8.

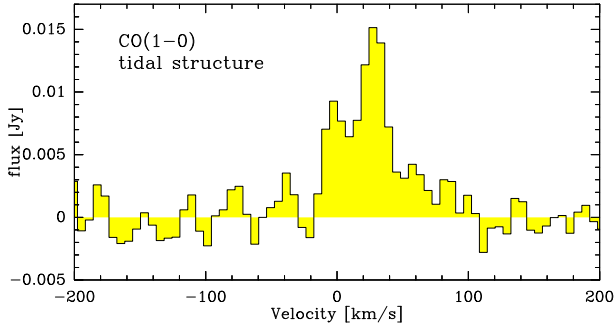


Fig. 8. PdB CO(1-0) spectrum of the tidal structure south-west of the merging nuclei of 4C12.50, integrated down to the 1σ flux level of Figure 5.

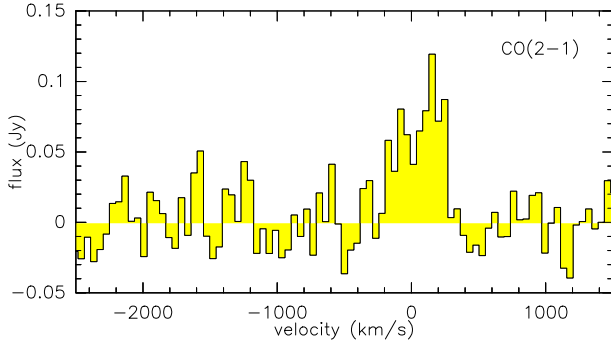


Fig. 9. IRAM 30 m telescope data of CO(2-1), comprising all regions where CO(1-0) was detected in the PdB data (i.e., the main component and the tidal structure).

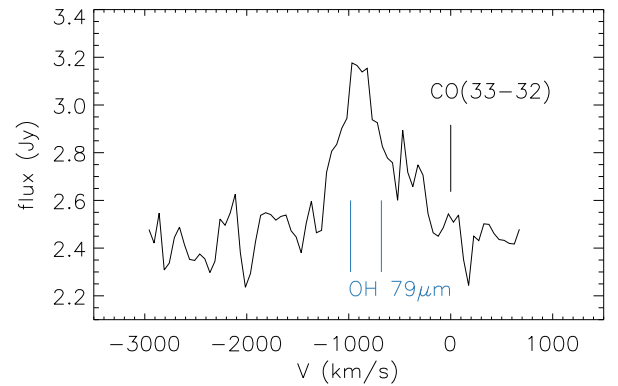
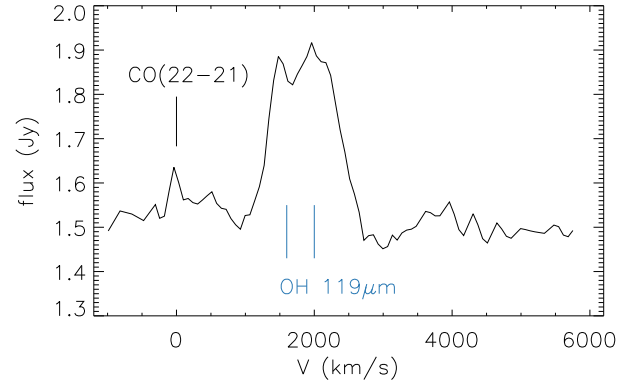
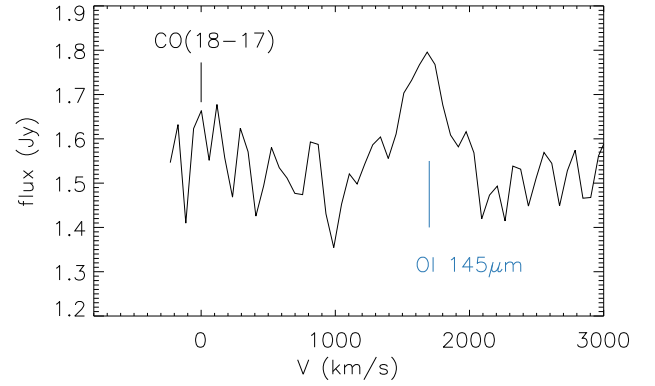
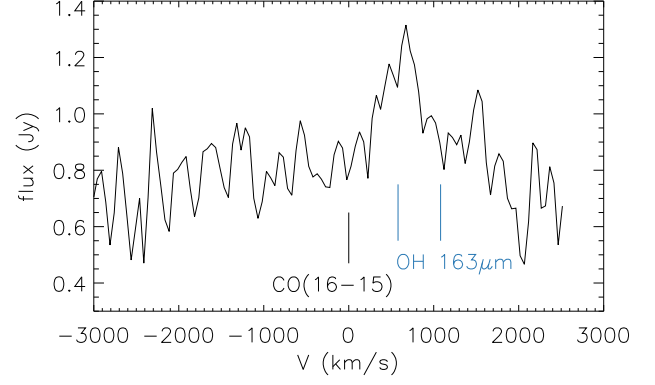


Fig. 10. PACS observations of 4C12.50 that cover the wavelengths of high- J CO spectral lines.

High- J CO emission was not detected with PACS, with a probable exception for the 22-21 transition (Figure 10): weak (3.5σ) signal was seen at restframe $118.58\mu\text{m}$, which was also seen by Spoon et al. (2013) and Veilleux et al. (2013) in their independent reductions of different sub-sets of the data. For the sake of completeness, we note that a spectrum of 4C12.50 showing no detection of CO lines was also acquired (OT1_pogle01_1) with SPIRE (Griffin et al., 2010). The limits used in this work (Table 1) are based on the wavelength-dependent instrumental sensitivity for the integration time of the SPIRE observations.

By means of a qualitative comparison of the SLED (Figure 11), we find that the high- J states of CO molecules are considerably less populated in 4C12.50 than those in local prototype AGN in which shock fronts and X-ray-photodissociation regions are likely to contribute to the gas excitation (e.g., NGC1068 and NGC6240; Krips et al., 2011; Hailey-Dunsheath et al., 2012; Spinoglio et al., 2012; Meijerink et al., 2013).

3.3. CO spectral line energy distribution fitting: cold vs. warm gas reservoir

To derive fundamental properties of the gas that is probed by our CO observations, we modeled the CO SLED with the radiative transfer code RADEX, assuming for simplicity that the flux that we detected over a line width of $\sim 520\text{ km s}^{-1}$ originates from a collection of clouds with same average properties and intrinsic line widths of 1 km s^{-1} (van der Tak et al., 2007). Further assuming that the cosmic microwave background temperature is 3.06 K and that the CO is excited by collisions with hydrogen and helium, we ran a grid of CO column density N_{CO} , CO kinetic temperature T_{kin} , and H_2 volume density n_{H_2} models to find those that best fit our data.

We considered intrinsic column densities in the range $5 \times 10^{14} - 5 \times 10^{17}\text{ cm}^{-2}$, corresponding to the beam-averaged CO column density in the chosen velocity step, divided by a filling factor of the beam by the clouds in the range 1-0.001. To compute this beam-averaged column density from the CO(1-0) observations, we used an H_2 gas mass of $1.0 \times 10^{10} M_{\odot}$, a CO abundance that is 10^4 times lower than that of the H_2 , and we equally divided the mass between 520 velocity bins. Having three unknown parameters and three line luminosity measurements, we obtained an exact solution for the model that best describes the molecular emission from the $J=1$, $J=2$, and $J=3$ upper states. It corresponds to a filling factor of 0.025, a CO kinetic temperature of 25 K , and an H_2 volume density of $1.5 \times 10^3\text{ cm}^{-3}$. In this solution, the CO(1-0)-emitting gas is out of local thermodynamic equilibrium (LTE): the CO(1-0) beam-corrected brightness temperature is 11 K , i.e., \sim two times lower than the H_2 kinetic temperature. The data of the CO(1-0) and CO(2-1) lines alone are compatible with a temperature of 7 K , for the same volume density but for a higher filling factor (0.092). The data of the CO(1-0) and CO(3-2) lines alone are compatible with a temperature as high as 32 K , again for the same volume density but for a lower filling factor (0.017).

To estimate the maximum warm gas mass that is probed by the CO, we calculated the maximum emission by molecules at high rotational states that is compatible with the observed SLED after fixing T_{kin} to 400 K . This ki-

netic temperature is marginally higher than the excitation temperature of the H_2 gas seen with *Spitzer* ($374 \pm 12\text{ K}$; Dasyra & Combes, 2011). For this computation, our free parameters were the H_2 volume density and the CO column density. Our column density grids were expanded to lower values than before. A model fitting the CO(18-17) and CO(22-21) data has an H_2 volume density of $2 \times 10^6\text{ cm}^{-3}$, and a CO column density of $5 \times 10^{13}\text{ cm}^{-2}$ (Figure 11). The mass of the warm H_2 as probed by the CO at 400 K is then equal to $2.5 \times 10^7 M_{\odot}$, or 0.0025 times the mass of the cold H_2 probed by the CO at 25 K , under the assumption that the emitting areas of the warm and the cold gas are identical. The 400 K gas mass would decrease if the CO(22-21) line luminosity were to be treated as an upper limit. If the warm gas were to be more tenuous, with an H_2 volume density of $1 \times 10^5\text{ cm}^{-3}$, then the CO column density would have to be below $5 \times 10^{14}\text{ cm}^{-2}$ for the CO(7-6) to CO(13-12) luminosity limits to be respected. In that case, the upper limit on the mass of the warm gas would be $2.5 \times 10^8 M_{\odot}$. In the likely presence of intermediate T_{kin} components, the mass estimate will again decrease.

To compare the gas and dust properties in the ambient medium, we produced the dust spectral energy distribution (SED) of 4C12.50 using our *Herschel* and IRAM continuum flux measurements (from this work, Table 2, Dasyra & Combes, 2012) together with data from the literature (Moshir et al., 1990; Steppe et al., 1995; Clements et al., 2010; Ostorero et al., 2010; Trippe et al., 2010; Guillard et al., 2012). The large scatter in the radio data is due to the time variability of the continuum. We fitted the SED by minimizing the χ^2 between the observations and a model consisting of multiple modified black body curves and a power law. We parameterized the flux emitted by each modified black body as $(M_{\text{dust}} \kappa_{\text{abs}}[\lambda_0]/D_L^2) (\lambda_0/\lambda)^\beta (2h\nu^3/c^2)/(e^{h\nu/kT} - 1)$, where M_{dust} is the dust mass at temperature T , $\kappa_{\text{abs}}[\lambda_0]$ is the dust absorption coefficient at the reference wavelength λ_0 , h is the Planck constant, and k is the Boltzmann constant. We opted for a reference wavelength accessible to PACS, $150\mu\text{m}$, and parameter values of $\beta=2.0$ and $\kappa_{\text{abs}}[150\mu\text{m}]=11.6\text{ cm}^2\text{ gr}^{-1}$. These parameter values reproduce the absorption coefficient of the Draine (2003) $R_V=3.1$, Milky Way dust model with an accuracy of 10% in the 70 to $1000\mu\text{m}$ range. We limited the temperature of the coldest dust SED component in the range 5-35 K. We also fixed the temperature of another component at 400 K , i.e., at the T_{kin} of the warm CO SLED component. A χ^2 minimization using the IDL MPFIT code indicated that three more components are needed to reproduce the observed SED (Figure 12). From the SED modeling, we found that the infrared luminosity of 4C12.50 is $2.4(\pm 0.1) \times 10^{12} L_{\odot}$, that the component that best fits the peak of the SED is at $T=40 \pm 3\text{ K}$, and that the component with the lowest temperature is at $19 \pm 5\text{ K}$.

The temperatures of the coldest dust SED components thus bracket the kinetic temperature of the cold CO SLED component ($25 \pm 8\text{ K}$). The SLED could also be reproduced up to CO(3-2) by a combination of two gas components with temperatures lower than or equal to those of the dust (e.g., 7 K and 40 K). Collisions with the ambient ISM could thus suffice to explain the excitation of the bulk of the CO molecules. A jet-induced shock does not have to be invoked instead.

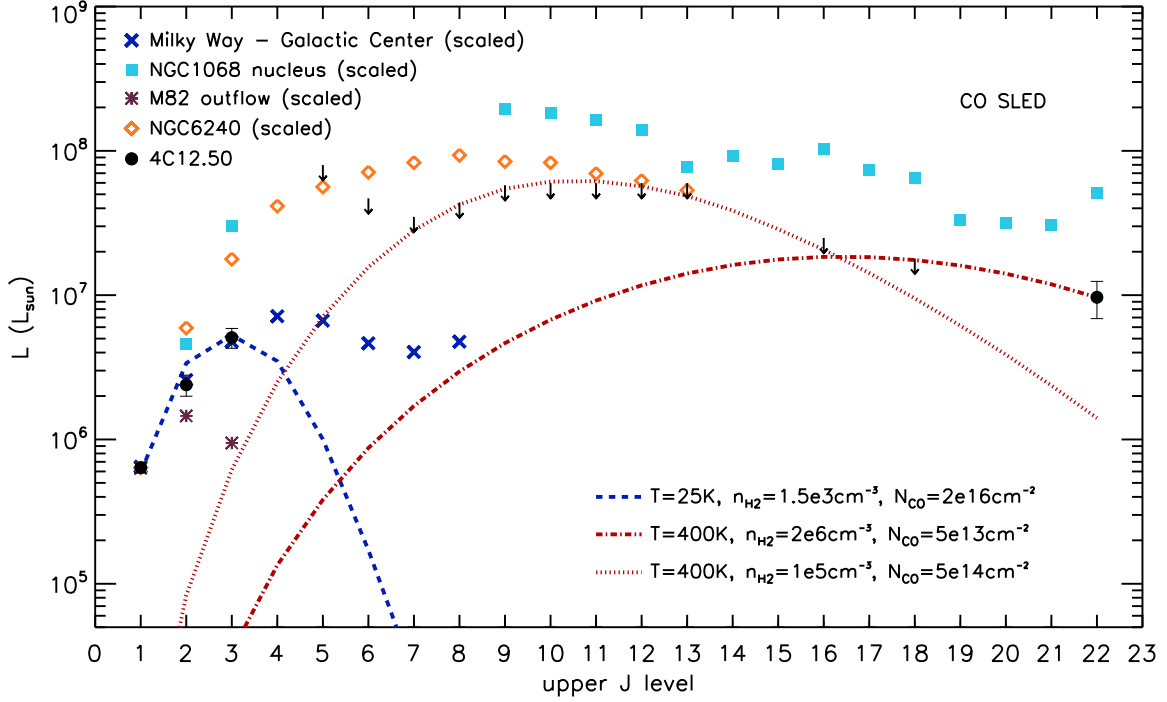


Fig. 11. CO SLED of 4C12.50 shown for transitions up to $J=22-21$. The CO(22-21) line is seen at 3.5σ levels. Based on our RADEX modeling, the SLED of the three lowest transitions is best fitted by gas with a kinetic temperature of 25 K (dashed line). Examples of RADEX models that are consistent with the *Herschel* data are also shown for gas with a kinetic temperature of 400 K, for a couple of column and volume density combinations (dashed-dotted and dotted lines). The SLEDs of other prototype sources are overplotted for comparison, normalized to $L_{\text{CO}(1-0)}(4\text{C12.50})/L_{\text{CO}(1-0)}$.

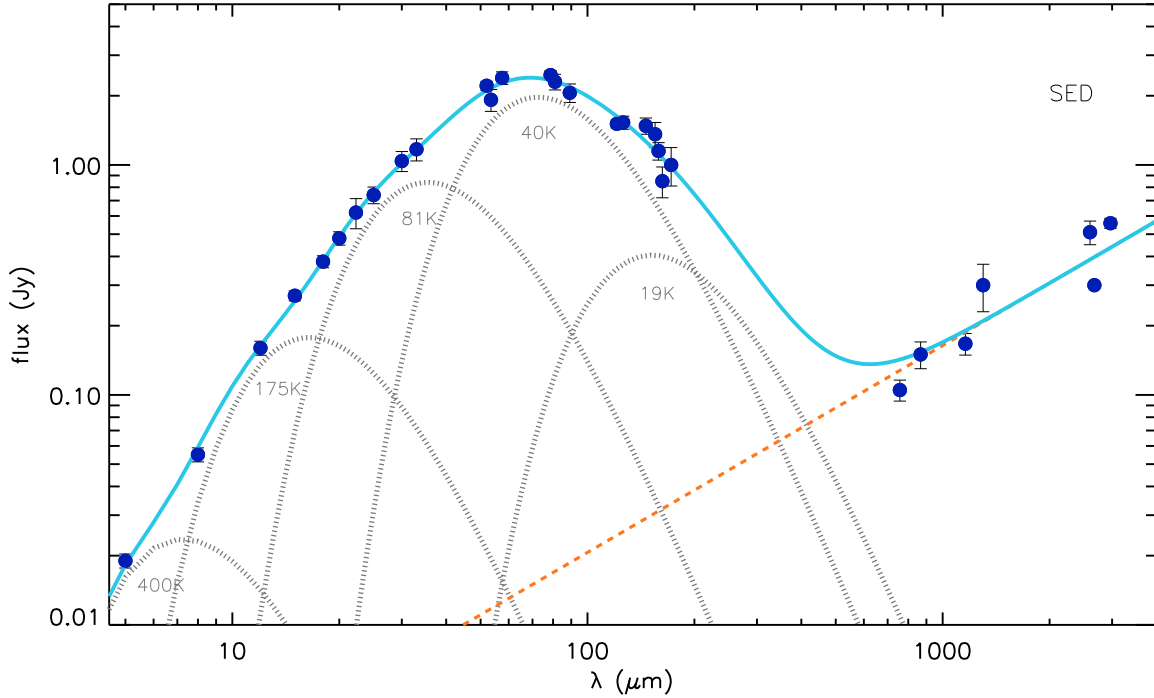


Fig. 12. Dust SED of 4C12.50 including continuum measurements from the new IRAM and *Herschel* data. The modified black body curves (with temperatures between 19 K and 400 K) that best fit the IR/sub-mm data are plotted with dotted lines. The dashed line is a synchrotron-related power law with an exponent of 0.9. The solid line corresponds to the sum of the flux of all components.

4. Discussion

4.1. Heating of the accelerated molecular gas with respect to the ambient medium

The results presented in Section 3 raise the question of how do the excitation properties of the accelerated molecular gas compare with those of the dynamically relaxed gas. From the *Spitzer* data, we know that the outflow has a warm component, carrying $5.2 \times 10^7 M_\odot$ of H_2 molecules at ~ 400 K (Dasyra & Combes, 2011). From a CO(2-3) absorption line that is due to clouds obscuring the millimeter continuum and moving at $-950(\pm 90) \text{ km s}^{-1}$, we know that colder molecules do exist in the outflow (Dasyra & Combes, 2012). Only a lower limit could be placed on their mass from the CO(2-3) data, because the absorption only probes the few lines of sight towards the millimeter continuum. The millimeter continuum is less extended than the radio continuum due to the steep power law that describes the emission from the jet lobes (Krichbaum et al., 1998, 2001, 2008), and the radio continuum is on its turn constrained to \sim ten hot spots with a radius of a few parsec each (Morganti et al., 2013b). The bulk of the cold entrained CO is thus likely to be found in lines of sight without a millimeter background, and it should be detected in emission. Its non-detection in our CO(1-0) PdB data now enables us to place an upper limit of $1.3 \times 10^8 M_\odot$ on the mass of cold entrained H_2 gas.

Putting all numbers together, we find that the mass ratio of warm (400 K) to cold (25 K) H_2 gas in the outflow is >0.40 . For the ambient medium, containing $1.0 \times 10^{10} M_\odot$ of H_2 molecules at 25 K and $1.4 \times 10^8 M_\odot$ of H_2 molecules at ~ 400 K (Section 3; Dasyra & Combes, 2011), the same ratio is only 0.014. A major result of this work is thus that the mass ratio of warm-to-cold H_2 gas is at least 29 times higher in the outflow than in the ambient medium.

Taking into account that a non-negligible fraction of the mid-infrared H_2 emission could be due to gas that was accelerated by the front shock but that is not accounted for in the outflow due to its low velocity, we conclude that the discrepancy in the warm-to-cold mass ratio could increase. Contrarily, adding the mass of the warm ambient H_2 probed by high- J CO lines to the mass of the warm ambient H_2 measured by *Spitzer* could decrease this discrepancy. Still, it would not alter our conclusion. Adding $2.5 \times 10^7 M_\odot$ of gas distributed in a dense 400 K component (in agreement with the high- J CO emission in Figure 11), would lead to a warm-to-cold H_2 mass ratio that is ≥ 24 times higher in the outflow than in the ambient medium. Even adding the maximum amount of 400 K gas that is compatible with the CO SLED, $2.5 \times 10^8 M_\odot$, would lead to a ratio that is ≥ 10 times higher in the outflow than in the ambient medium. Likewise, our conclusion is robust against the use of another α factor, or the use of different α factors for the entrained and ambient gas (see, e.g., Papadopoulos et al., 2012). The latter choice can be justified because the CO intensity to H_2 mass conversion scales with $T_{\text{kin}}^{-1}(n_{H_2})^{1/2}$ for virialized clouds (Maloney et al., 1988; Weiss et al., 2001). Figure 13, showing the dependence of the warm-to-cold H_2 mass ratio on the α factor, indicates that there is no combination of acceptable α and warm gas mass values that could make the ratio in the ambient medium agree with that in the outflow. Instead, the ratio in the outflow is at least 3–30 times higher than that in the ambient medium in the entire parameter space.

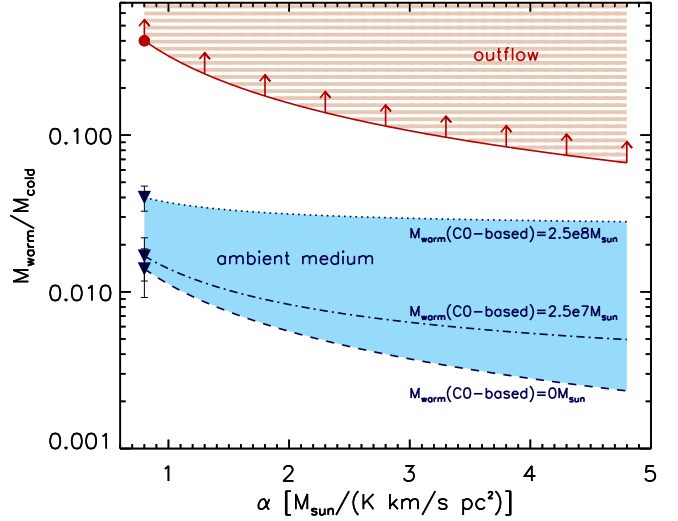


Fig. 13. Warm-to-cold gas mass ratio as a function of the α conversion factor. The circle shows the ratio's lower limit in the outflow for $\alpha = 0.8 M_\odot / (\text{K km s}^{-1} \text{ pc}^2)$. The solid line shows how this lower limit decreases as α approaches values thought appropriate for the Milky Way. This curve brackets the range of all acceptable $M_{\text{warm}}/M_{\text{cold}}$ values in the outflow (hatched area), under the assumption that the mass of the 400 K outflowing gas probed by the CO is negligible with respect to that directly probed by the H_2 . For the ambient medium, the measured ratio (triangles) and its dependence on α (non-solid lines) are given for different warm gas content scenarios: when only the mass of the 400 K H_2 gas directly seen by *Spitzer* is used (dashed line), and when the mass of another CO-based 400 K gas component is added. The dashed-dotted line uses an additional mass of $2.5 \times 10^7 M_\odot$ distributed in clouds of $2 \times 10^6 \text{ cm}^{-3}$ (as in the dashed-dotted CO SLED component in Figure 11). The dotted line uses an additional mass of $2.5 \times 10^8 M_\odot$ distributed in clouds of $1 \times 10^5 \text{ cm}^{-3}$ (as in the dotted CO SLED component in Figure 11). This line constrains the upper range of acceptable $M_{\text{warm}}/M_{\text{cold}}$ values in the ambient medium (solid area).

Our results constitute direct evidence that the accelerated molecular gas can be heated⁴ to the point of being inefficient to form new stars, and that it can be detected even though the cooling timescales can be considerably shorter than the outflow propagation timescales (Guillard et al., 2012), possibly thanks to the enhancement of turbulence on individual-cloud scales (Nesvadba et al., 2011). Papadopoulos et al. (2008) and Ogle et al. (2010) previously attributed the overall strong emission by CO molecules in states of intermediate rotational number and by H_2 molecules in states of low rotational number to shock excitation by radio jets.

⁴ Heating of the molecular gas, leading to excitation at high rotational states, could be one of the reasons why absorption of the mm continuum by outflowing molecules is not (reliably) detected in CO(0-1) in the PdB data while it was detected in CO(2-3) in the single-dish data. Alternatively, absorption in CO(0-1) may not be seen if it is diluted in CO(1-0) emission. A similar scenario may not hold for CO(2-3) and CO(3-2) depending, e.g., on the size and the geometry of the emitting regions. Changes with time in the relative position of the foreground clouds and the background source leading to changes in the covering factor, or changes with time in the millimeter continuum flux could also justify this result.

4.2. Impact of the outflow on the galaxy

The outflow could affect the future evolution of 4C12.50 via gas heating or gas expulsion. While the effects of heating are uncertain, we observe that the feedback mechanism has not had the time to reach and excite a large fraction of the CO reservoir.

To test the role of gas expulsion, we compute the mass outflow rate, \dot{M}_{out} , which is equal to $M_{out}V_{out}d^{-1}$. We revise the flow rate of warm gas presented in Dasyra & Combes (2011) from $130 M_{\odot}\text{yr}^{-1}$ to $230 M_{\odot}\text{yr}^{-1}$, using identical values for the outflow velocity V_{out} (640 km s^{-1}) and mass M_{out} ($5.2 \times 10^7 M_{\odot}$), but assuming that the entrained gas is within a distance d of 150 pc from the radio core (Morganti et al., 2013b). The flow of cold gas could carry up to $570 M_{\odot}\text{yr}^{-1}$, under the assumption that the entrained CO and the entrained H_2 have the same average velocity. This assumption is not in conflict with the CO(2-3) detection at -950 km s^{-1} (Dasyra & Combes, 2012), which only probes the motions of some outflowing clouds: those situated between us and the radio core. For both gas phases, the total mass flow rate is in the range $230\text{--}800 M_{\odot}\text{yr}^{-1}$.

However, only a part of this gas could be lost to the intergalactic medium. The escape velocity at 150 pc from the west nucleus of 4C12.50 is 700 km s^{-1} , when assuming an isothermal sphere distribution for the visible baryonic matter and when using a stellar velocity dispersion of 170 km s^{-1} and a half-light radius of 2.6 kpc (Dasyra et al., 2006a). The escape velocity will increase to 800 km s^{-1} when the mass in the east nucleus of 4C12.50 is accounted for. From the H_2 velocity distribution in the *Spitzer* data, less than 30% of the gas could be lost to the intergalactic medium. Most of the accelerated and heated gas will fountain back to a disk within a few dynamical timescales. The maximum mass loss rate would be $\lesssim 240 M_{\odot}/\text{yr}$, and the minimum depletion timescale of the reservoir $\gtrsim 4 \times 10^7$ yrs. The depletion timescale could increase further and exceed the typical values for AGN duty cycles when the mass in the dark matter halo(s) is taken into account.

Any gas expulsion could be moderated or counteracted by a potential inflow of gas from the southern tidal tail. At the projected distance of the tail, ~ 10 kpc, the escape velocity from the visible baryonic matter is of order $200\text{--}300 \text{ km s}^{-1}$, i.e., higher than the typical rotational velocities of spiral arms. Given that the line-of-sight velocity of the tidal tail is $< 40 \text{ km s}^{-1}$, gas could be captured and fed to the western nucleus.

We thus postulate that both gas expulsion and heating are likely to temporarily delay but unlikely to entirely suppress star formation in 4C12.50.

4.3. Driving mechanism of the outflow

Power and momentum arguments are typically invoked for the evaluation of the outflow driver. The flow kinetic luminosity can be computed from the product $0.5 M_{out} V_{out}^3 d^{-1}$. For the M_{out} , V_{out} , and d values discussed in Section 4.2, the kinetic luminosity of the warm entrained gas that is probed by the H_2 is $3 \times 10^{43} \text{ erg s}^{-1}$. Adding the maximum amount of cold outflowing gas that could be probed by the CO would place the kinetic luminosity upper limit to $1 \times 10^{44} \text{ erg s}^{-1}$. The luminosity radiated by the outflowing gas in the purely rotational H_2 lines, $4 \times 10^{41} \text{ erg s}^{-1}$

(Dasyra & Combes, 2011), is negligible with respect to the outflow kinetic luminosity. The luminosity radiated in CO lines is even lower than that radiated in H_2 lines.

According to Veilleux et al. (2009), half of the infrared luminosity of this source can be ascribed to its AGN and half to its starburst, with an uncertainty of $\sim 50\%$ on either fraction. The dust-based star-formation-rate estimate is then $400 M_{\odot}/\text{yr}$ (Kennicutt, 1998). The power released by supernovae (SN) is $10^{44} \text{ erg s}^{-1}$, under the assumption that for every hundred solar masses forming there is one SN (e.g., in the Kroupa, 2001, initial mass function context), ejecting material with a kinetic energy of 10^{51} erg . This energy is insufficient to drive the flow unless a very large fraction (30-100%) of it is converted into the outflow kinetic luminosity.

The luminosity of the AGN, like that of the starburst, is estimated to be $5 \times 10^{45} \text{ erg s}^{-1}$. The force exerted to the gas by radiation pressure is then 5-18 times lower than the outflow momentum rate, when the latter is approximated by the product $\dot{M}_{out} V_{out}$ (Combes et al., 2013). The momentum rate boost needed for the gas acceleration could occur with the aid of energy-conserving gas expansion or multiple photon scatterings in high optical depth regions (Faucher-Giguère & Quataert, 2012). For these mechanisms, the compact-source geometry of the AGN is advantageous.

The AGN jet constitutes a generous power source, capable of driving the flow. The radio cavity kinetic luminosity is estimated from its 178 MHz flux to be $3 \times 10^{45} \text{ erg s}^{-1}$ (Guillard et al., 2012). The most significant argument in favor of the radio jet remains the location of the HI outflow, at the tip of the southern radio hot spot (Morganti et al., 2013b). The young age of the jet, limited to $< 10^5$ yrs (Lister et al., 2003), could explain why only a small amount of the CO is affected by the feedback.

4.4. Implications for future observations

Recent hydrodynamic simulations indicate that gas heating could be common in AGN outflows: the effects of jets and radiation-driven ultra-fast winds on the ISM can be comparable only $10^4\text{--}10^5$ years after the onset of the feedback activity (Wagner & Bicknell, 2011; Wagner et al., 2013), when both mechanisms drive bubbles of similar flow structure and dynamics.

If heating of the accelerated molecular gas is common, then the detection of outflows could be easier in intermediate- J CO lines than in low- J CO lines, facilitating the discovery of outflows in the distant Universe: at $z \sim 1$ or higher, for example, ALMA could probe outflows of comparable mass to those presently detected at 100 Mpc with the PdB. Moreover, the acquisition of infrared data alongside millimeter data could be valuable for the systematic discovery and reliable mass determination of outflows. With ALMA operating in full-array mode in \sim two years and with the *James Webb* Space Telescope coming up beyond 2018, these goals will be achievable for most systems of interest in the local Universe. At 100 Mpc, ALMA is designed to detect $5 \times 10^5 M_{\odot}$ outflows of 10 K gas in CO(1-0). The JWST is designed to reach the same limit for the ~ 100 K gas probed by $\text{H}_2(0-0)\text{S}(1)$. For typical outflow radial extents of a few hundred pc, this common detection threshold corresponds to an outflow rate of $\sim 1 M_{\odot}\text{yr}^{-1}$, comparable to the star formation rate in local spirals.

5. Conclusions

We used IRAM PdB, 30 m telescope, and *Herschel* Space Telescope data to study the content, excitation, and kinematic properties of the molecular gas in the outflow and in the ambient medium of a local prototype radio-loud, ultraluminous-infrared galaxy, 4C12.50 (also known as IRAS13451+1232). We specifically looked for gas heating and expulsion signatures, i.e., characteristic of the two feedback-related processes that can delay star formation. Combining new and previous observations, we found evidence for both processes taking place, and we drew the following main conclusions.

- The CO(1-0) emission spatially consists of a newly discovered tidal tail, which extends out to 12 kpc southwest of the nucleus, and a main component, which is marginally resolved within the beam radius (4.2 kpc). A shift in the location of the maximum emission with velocity indicates that the main component could be tracing either two merging nuclei or a rotating disk. Its reservoir contains $1.0(\pm 0.1) \times 10^{10} M_{\odot}$ of cold H_2 gas for $\alpha = 0.8 M_{\odot}/(K km s^{-1} pc^2)$.
- The CO SLED, which is primarily tracing the ambient gas in 4C12.50, is very similar with that of the Milky Way gas for low- J numbers. Fitting of the CO SLED with RADEX indicates that the gas mass probed by CO molecules at 400 K is less than 0.025 times the gas mass probed by CO molecules at 25 K. Likewise, the H_2 gas mass probed by CO molecules at 400 K is less than 1.7 times the mass of the 400 K gas probed by the purely rotational H_2 lines in the mid-infrared.
- In the outflow, the mass of the cold (25 K) H_2 gas is $< 1.3(\pm 0.1) \times 10^8 M_{\odot}$, i.e., at most twice as high as the mass of the warm (400 K) H_2 gas emitting in the mid-infrared. By combining the H_2 -based mass flow rate measurement from the mid-infrared data, $230 M_{\odot}/yr$, with the CO-based mass flow rate upper limit from the mm data, $570 M_{\odot}/yr$, we conclude that the feedback mechanism(s) could be accelerating up to $800 M_{\odot}/yr$ of molecular gas for an outflow radius of 150 pc.
- A low fraction of the outflowing gas ($< 30\%$ when ignoring dark matter) could escape the system and be lost to the intergalactic medium. Any mass loss could be moderated or counteracted by a potential inflow of gas from the tidal tail containing $3.3(\pm 0.3) \times 10^8 M_{\odot}$ of cold H_2 . The star formation in the host of 4C12.50 is likely to be delayed, but not entirely suppressed by the feedback.
- The mass ratio of warm-to-cold H_2 gas is elevated in the outflow with respect to the ambient medium by a factor of $\gtrsim 30$ for $\alpha = 0.8 M_{\odot}/(K km s^{-1} pc^2)$. The conclusion that the accelerated molecular gas is heated is robust against two main sources of uncertainty: the chosen α conversion factor, and the mass of the warm gas probed by the CO. While the discrepancy will be lower for higher values of either parameter, there is no combination of acceptable parameter values that could make the warm-to-cold gas mass ratio in the ambient medium reach that in the outflow.
- A scenario in which outflows could be probed by a different CO SLED than the rest of the ISM is likely. It remains to be tested with sub-millimeter observations.

Acknowledgements. K. M. D. thanks F. Casoli, O. La Marle, and M. Lozach for making this project possible by means of a French Space

Agency (Centre National d'Etudes Spatiales; CNES) fellowship. Our work is based on data obtained with the facilities of IRAM, which is supported by INSU/CNRS (France), MPG (Germany), and IGN (Spain), and on data obtained with the *Herschel* Space Telescope, which is an ESA space observatory with science instruments provided by European-led principal investigator consortia and with important participation from NASA.

References

- Aalto, S., Garcia-Burillo, S., Muller, S., et al. 2012, *A&A*, 537, 44
 Alatalo, K., Blitz, L., Young, L. M., et al. 2011, *ApJ*, 735, 88
 Batcheldor, D., Tadhunter, C., Holt, J., et al. 2007, *ApJ*, 661, 70
 Bernardi, M., Meert, A., Sheth, R. K., et al. 2013, *MNRAS*, 436, 697
 Birnboim, Y., Dekel, A., & Neistein, E. 2007, *MNRAS*, 380, 339
 Booth, C. M., & Schaye, J. 2009, *MNRAS*, 398, 53
 Bower, R. G., Benson, A. J., Malbon, R., et al. 2006, *MNRAS*, 370, 645
 Cantalupo, S., Lilly, S. J., & Haehnelt, M. G. 2012, *MNRAS*, 425, 1992
 Carter, M., Lazareff, B., Maier, D. et al. 2012, *A&A*, 538, 89
 Ciccone, C., Feruglio, C., Maiolino, R., et al. 2012, *A&A*, 543, 99
 Ciccone, C., Maiolino, R., Sturm, E., et al. 2014, *A&A*, 562, 21
 Combes, F., Garcia-Burillo, S., Casasola, V. et al. 2013, *A&A*, 558, A124
 Clements, D. L., Dunne, L., & Eales, S. 2010, *MNRAS*, 403, 274
 Croft, S., van Breugel, W., de Vries, W., et al. 2006, *ApJ*, 647, 1040
 Croton, D. J., Springel, V., White, S. D. M., et al., 2006, *MNRAS*, 367, 864
 Dasyra, K. M., Tacconi, L. J., Davies, R. I., et al. 2006a, *ApJ*, 638, 745
 Dasyra, K. M., Tacconi, L. J., Davies, R. I., et al. 2006b, *ApJ*, 651, 835
 Dasyra, K. M., & Combes, F. 2011, *A&A*, 533, L10
 Dasyra, K. M., & Combes, F. 2012, *A&A*, 541, L7
 Debuhr, J., Quataert, E., & Ma, C.-P. 2012, *MNRAS*, 420, 2221
 Dekel, A., & Birnboim, Y. 2008, *MNRAS*, 383, 119
 Downes, D., & Solomon, P. M. 1998, *ApJ*, 507, 615
 Draine, B. T., 2003, *ARA&A*, 41, 241
 Eckart, A., Cameron, M., Genzel, R., et al. 1990, *ApJ*, 365, 522
 Fabian, A. C. 2012, *ARA&A*, 50, 455
 Faucher-Giguère, C.-A. & Quataert, E. 2012, *MNRAS*, 425, 605
 Feruglio, C., Maiolino, R., Piconcelli, E., et al. 2010, *A&A*, 518, L155
 Fischer, J., Sturm, E., González-Alfonso, E., et al. 2010, *A&A*, 518, L41
 Fu, H., & Stockton, A. 2009, *ApJ*, 690, 953
 Gaibler, V., Khochfar, S., Krause, M., & Silk, J. 2012, *MNRAS*, 425, 438
 Golombek, D., Miley, G. K., & Neugebauer, G. 1988, *AJ*, 95, 26
 Granato, G. L., De Zotti, G., Silva, L., Bressan, A., & Danese, L. 2004, *ApJ*, 600, 580
 Griffin, M. J., Abergel, A., Abreu, A. et al. 2010, *A&A*, 518, L3
 Guillard, P., Ogle, P., Emonts, B., et al. 2012, *ApJ*, 747, 95
 Hailey-Dunsheath, S., Sturm, E., Fischer, J., et al. 2012, *ApJ*, 755, 57
 Heckman, T. M., Lehnert, M. D., Strickland, D. K., & Armus, L. 2000, *ApJS*, 129, 493
 Holt, J., Tadhunter, C. N., & Morganti, R. 2008, *MNRAS*, 387, 639
 Holt, J., Tadhunter, C. N., Morganti, R., & Emonts, B. H. C. 2011, *MNRAS*, 410, 1527
 Ivison, R. J., Smail, I., Amblard, A., Arumugam, V., De Breuck, C. et al. 2012, *MNRAS*, 425, 1320
 Kennicutt, R. C. 1998, *ApJ*, 498, 541
 Krichbaum, T. P., Alef, W., Witzel, A., et al., 1998, *A&A* 329, 873
 Krichbaum, T. P., Graham, D., Witzel, A., et al. 2001, *ASPC*, 250, 184
 Krichbaum, T. P., Lee, S. S., Lobanov, A. P., et al. 2008, *ASPC*, 386, 186
 Krips, M., Martín, S., Eckart, A., et al. 2011, *ApJ*, 736, 37
 Kroupa, P. 2001, *MNRAS*, 322, 231
 Leon, S., Eckart, A., Laine, S. et al. 2007, *A&A*, 473, 747
 Lípári, S., Mediavilla, E., Daz, R. J., et al. 2004, *MNRAS*, 348, 369
 Lister, M. L., Kellermann, K. I., Vermeulen, R. C., et al. 2003, *ApJ*, 584, 135
 Maloney, P., & Black, J. H. 1988, *ApJ*, 325, 389
 Martin, C. L. 2005, *ApJ*, 621, 227
 Meijerink, R., Kristensen, L. E., Weiss, A. et al. 2013, *ApJ*, 762, L16
 Morganti, R., Tadhunter, C. N., & Oosterloo, T. A. 2005, *A&A*, 444, L9

- Morganti, R., Frieswijk, W., Oonk, R. J. B., Oosterloo, T., & Tadhunter, C. 2013, *A&A*, 552, L4
- Morganti, R., et al. 2014, *Science*, 341, 1082
- Moshir, M., Kopan, G., Conrow, T., et al., 1990 IRAS F.C "The Faint Source Catalog, Version 2.0", 0000
- Nesvadba, N., Boulanger, F., Lehnert, M., et al. 2011 *A&A*, 536, L5
- Ogle, P., Boulanger, F., Guillard, P., 2010, *ApJ*, 724, 1193
- Ostorero, L., Moderski, R., Stawarz, L., et al. 2010, *ApJ*, 715, 1071
- Ott, S. 2010, *ASP Conference Series*, 434, 139
- Papadopoulos, P. P., Kovacs, A., Evans, A. S., & Barthel, P. 2008, *A&A*, 491, 483
- Papadopoulos, P. P., van der Werf, P., Xilouris, E., Isaak, K., & Gao, Y. 2012, *ApJ*, 751, 10
- Pilbratt, G.L., Riedinger, J.R., Passvogel, T. et al. 2010, *A&A*, 518, L1
- Poglitsch, A., Waelkens, C., Geis, N. et al. 2010, *A&A*, 518, L2
- Rangwala, N., Maloney, P. R., Glenn, J., 2011, *ApJ*, 743, 94
- Rupke, D. S., Veilleux, S., & Sanders, D. B. 2005, *ApJ*, 632, 751
- Rupke, D. S. N., & Veilleux, S. 2011, *ApJ*, 729, L27
- Sajina, A., Yan, L., Lutz, D., et al. 2008, *ApJ*, 683, 659
- Sakamoto, K., Ho, P. T. P., Peck, A. B. 2006, *ApJ*, 644, 862
- Sakamoto, K., Aalto, S., Wilner, D. J. 2009, *ApJ*, 700, L104
- Sanders, D. B., & Mirabel, I. F. 1996, *ARA&A*, 34, 749
- Silk, J. 2013, *ApJ*, 772, 112
- Solomon, P. M., Downes, D., Radford, S. J. E., & Barrett, J. W. 1997, *ApJ*, 478, 144
- Somerville, Rachel S., Hopkins, Philip F., Cox, T. J., et al. 2008, *MNRAS*, 391, 481
- Spinoglio, L., Pereira-Santaella, M., Busquet, G., et al. 2012, *ApJ*, 758, 108
- Spoon, H. W. W., Farrah, D., Leboutellier, V., et al. 2013, *ApJ*, 775, 127
- Steppe, H., Jeyakumar, S., Saikia, D.J., & Salter, C.J. 1995, *A&AS*, 113, 409
- Sturm, E., González-Alfonso, E., Veilleux, S., et al. 2011, *ApJ*, 733, L16
- Trippe, S., Neri, R., Krips, M., et al. 2010, *A&A*, 515, 40
- Tsai, A.-L., Matsushita, S., Kong, A. K. H. et al. 2012, *ApJ*, 752, 38
- van Breugel, W., Filippenko, A. V., Heckman, T., & Miley, G. 1985, *ApJ*, 293, 83
- van der Tak, F.F.S., Black, J.H., Schöier, F.L., Jansen, D.J., & van Dishoeck, E.F., 2007, *A&A* 468, 627
- Veilleux, S., Rupke, D., Kim, D. C., et al. 2009, *ApJS*, 182, 628
- Veilleux, S., Meléndez, M., Sturm, E., et al. 2013, *ApJ*, 776, 27
- Wagner, A. Y., & Bicknell, G. V. 2011, *ApJ*, 728, 29
- Wagner, A. Y., Umemura, M., & Bicknell, G. V. 2013, *ApJ*, 763, L18
- Weiss, A., Neininger, N., Hüttemeister, S., & Klein, U. 2001, *A&A*, 365, 571
- Weiss, A., Walter, F., & Scoville, N. Z. 2005, *A&A*, 438, 533
- Westmoquette, M. S., Clements, D. L., Bendo, G. J., & Khan, S. A. 2012, *MNRAS*, 424, 416
- Wiklind, T., & Combes, F. 1997, *A&A*, 324, 51